PAPER

Nanohybrid structured RuO_2/Mn_2O_3/CNF as a catalyst for Na–O_2 batteries

View the article online for updates and enhancements.

IOP ebooks™

Bringing you innovative digital publishing with leading voices to create your essential collection of books in STEM research.

Start exploring the collection - download the first chapter of every title for free.

Nanohybrid structured RuO$_2$/Mn$_2$O$_3$/CNF as a catalyst for Na–O$_2$ batteries

Mohammad Fathi Tovini, Bhushan Patil, Cevriye Koz, Tamer Uyar and Eda Yılmaz

Institute of Materials Science and Nanotechnology, National Nanotechnology Research Center, Bilkent University, Ankara 06800, Turkey

E-mail: yilmaz@unam.edu.tr

Abstract

A 3D RuO$_2$/Mn$_2$O$_3$/carbon nanofiber (CNF) composite has been prepared in this study by a facile two step microwave synthesis, as a bi-functional electrocatalyst towards oxygen reduction reaction (ORR) and oxygen evolution reaction (OER). RuO$_2$ nanoparticles with the mean size of 1.57 nm are uniformly distributed on Mn$_2$O$_3$ nano-rods grown on electrospun CNFs. The electrocatalytic activity of the composites are investigated towards ORR/OER under alkaline condition. The ternary RuO$_2$/Mn$_2$O$_3$/CNF composite showed superior ORR activity in terms of onset potential (0.95 V versus RHE) and Tafel slope (121 mV dec^{-1}) compared to its RuO$_2$/CNF and Mn$_2$O$_3$/CNF counterparts. In the case of OER, the RuO$_2$/Mn$_2$O$_3$/CNF exhibited 0.34 V over-potential value measured at 10 mA cm^{-2} and 52 mV dec^{-1} Tafel slope which are lower than those of the other synthesized samples and as compared to state of the art RuO$_2$ and IrO$_x$ type materials. RuO$_2$/Mn$_2$O$_3$/CNF also exhibited higher specific capacity (9352 mAh g$_{carbon}^{-1}$) than CNF (1395 mAh g$_{carbon}^{-1}$), Mn$_2$O$_3$/CNF (3108 mAh g$_{carbon}^{-1}$) and RuO$_2$/CNF (4859 mAh g$_{carbon}^{-1}$) as the cathode material in Na–O$_2$ battery, which indicates the validity of the results in non-aqueous medium. Taking the benefit of RuO$_2$ and Mn$_2$O$_3$ synergistic effect, the decomposition of inevitable side products at the end of charge occurs at 3.838 V versus Na/Na$^+$ by using RuO$_2$/Mn$_2$O$_3$/CNF, which is 388 mV more cathodic compared with CNF.

Supplementary material for this article is available online

Keywords: RuO$_2$/Mn$_2$O$_3$/CNF, 3D composite, oxygen reduction reaction, oxygen evolution reaction, Na–O$_2$ batteries

(Some figures may appear in colour only in the online journal)

1. Introduction

Metal-O$_2$ batteries have attracted considerable research attention over Li-ion batteries due to their higher theoretical energy density [1, 2]. Li–O$_2$ batteries are the most studied metal-O$_2$ systems to date, in which the cell electrochemistry basically relies on the reversible formation of Li$_2$O$_2$ as the main discharge product during cycling. However, the insulating nature of Li$_2$O$_2$ induces large over-potential (>1 V) and low Coulombic efficiency to the system. In this regard, Na–O$_2$ batteries are decent substitutes because deposition of NaO$_2$ during oxygen reduction reaction (ORR) results in much lower charging over-potential (typically <0.2 V) during oxygen evolution reaction (OER) because of facilitated OER kinetics of superoxide species. However, these cells suffer from a considerably lower theoretical energy density (1105 Wh kg^{-1} based on NaO$_2$) than Li–O$_2$ cells (3500 Wh kg^{-1} based on Li$_2$O$_2$) and highly active nature of NaO$_2$ triggers the formation of side products and precipitous over-potential increase at the end of OER [3–7]. Therefore, a rational design of a catalyst is required for feasibility of stationary applications of these systems.

Although Pt and its alloys are well known catalysts for ORR, their moderate OER activity, high price and surface

poisoning hinder their application as bi-functional electrocatalysts for these reactions [8]. The first row transition metal oxides, like NiO_x and CoO_x are promising alternative catalysts for ORR due to their reasonably comparable catalytic activity to Pt, lower cost, high stability and abundance in the nature [9]. Manganese oxides (MnO_x like α-, β-, γ-, δ-MnO_2, Mn_2O_3 and Mn_3O_4) have been widely investigated as outstanding ORR catalysts due to several characteristics of Mn including: its oxidation state change between $+2$, $+3$ and $+4$ near the equilibrium ORR potential which facilitates oxygen atoms exchange in relevant potentials, low toxicity, high chemical stability and earth abundance and potential for large scale energy applications [10–13]. However, the poor electronic conductivity and the relatively low OER kinetics of MnO_x limits its application as a bi-functional electrocatalyst and needs to be considered for future applications. To address the low electronic conductivity of MnO_x, several researches have been attempted to combine it with highly conductive carbonaceous materials like graphene, carbon nanotubes and porous carbon [14–16]. Among all, electrospun carbon nanofibers (CNF) have been considered as promising backbone for MnO_x to improve the charge exchange due to its high surface area, excellent electrical conductivity, mechanical property and low cost of synthesis [17]. However, to the best of our knowledge, CNF has not been studied as a matrix for MnO_x deposition for ORR/OER application.

In order to deal with the low OER activity of MnO_x, composite materials containing MnO_x and metal/oxides (like Au, Ti, TiO_2, Co_3O_4, Fe_2O_3 etc) have been proposed [18–22]. Ruthenium based oxides (RuO_x) have been frequently reported as high electronically conductive catalysts especially for OER based electrochemistry [23–25]. In this regard, Lee *et al* showed the OER catalytic activity of RuO_2 in both acidic and basic media [26]. Also recently, Bhowmik *et al* confirmed the OER activity of RuO_2 nanowires grown on carbonnitride in all pH values, including acidic (pH = 0), neutral (pH = 7) and alkaline (pH = 14) solutions [27]. For these reasons, the MnO_x/RuO_x combination has been achieved by different research groups as a bi-functional catalyst for ORR/ OER for diverse applications [28–30]. However, the lack of a rational 3D structure design consisting of a highly electronic conductive path in the core to supply electric charge and maintain the mechanical stiffness of the structure can be realized in these works. Such a design has been extensively investigated for the energy conversion and storage applications. They include 3D carbon/SnO_x [31], CNT/MO (M = Co, Zn, Mn) [32], CNF/Fe_3O_4 [33], SnO_2/Co_3O_4 nano fiber-coated graphene [34] etc.

Herein, we first optimize a rational 3D design of RuO_2/Mn_2O_3/CNF (RMC) bi-functional catalyst for ORR/ OER in alkaline aqueous media and in the second step, the optimized samples are implemented as the cathode material for Na–O_2 batteries. RMC has been prepared through a facile two-step microwave synthesis, in which RuO_2 nano-particles were attached on the as synthesized Mn_2O_3 nano-rods coated electrospun CNF (figure 1). Electrospun CNFs provide an optimal surface for the 3D structure to grow and the electrochemical results confirmed that the 3D RMC exhibits
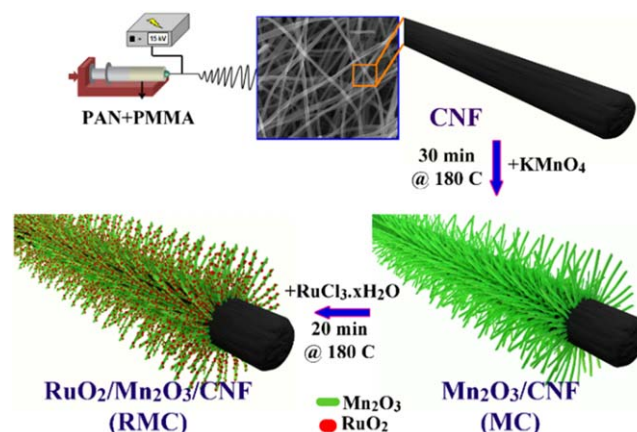

Figure 1 Schematic illustration of 3D RMC composite preparation. Electrospun-CNF was used as the backbone for Mn_2O_3 nanorods deposition in the first hydrothermal step. Then, RMC was prepared during the second hydrothermal step by using MC as the template for RuO_2 nano-particles deposition.

improved ORR/OER catalytic activity compared to its RuO_2/CNF (RC) and Mn_2O_3/CNF (MC) counterparts, which demonstrates that RMC offers a competitive alternative to the already available ORR/OER catalysts.

2. Experimental

2.1. Preparation of Mn₂O₃/CNF, RuO₂/CNF and RuO₂/Mn₂O₃/CNF

In the first step, Mn_2O_3/CNF (MC) composites were prepared by a facile microwave synthesis method. Typically, 20 mg of electrospun CNF (fabrication details in supplementary information) was dispersed in 20 ml DI water by 10 min sonication. Then, different amounts of $KMnO_4$ were mixed with the CNF dispersion and stirred in the room temperature for 30 min. The above dispersions were added to the vessels and the microwave-assisted hydrothermal reactions were performed at 180 °C for 30 min in the microwave synthesis reactor (Anton Paar Monowave 300). The amount of $KMnO_4$ was adjusted to 0.125, 0.25 and 0.5 mmol to result MC1, MC2 and MC3 samples, respectively. After the reactions were performed, MC samples were washed and centrifuged with DI water and ethanol for several times and dried in an oven at 60 °C for overnight. Finally, the samples were annealed for 1 h in 150 °C in the air atmosphere.

For RMC preparation, 20 mg MC2 was dispersed in 20 ml DI water by 5 min sonication and different amounts of $RuCl_3.xH_2O$ were mixed with the solution by stirring for 30 min. Then, the resulting mixtures were added into the vessels and put in the microwave synthesis reactor at 180 °C for 20 min. The amount of $RuCl_3.xH_2O$ was adjusted to 0.01, 0.025 and 0.04 mmol to result RMC1, RCM2 and RMC3 samples, respectively. Figure 1 shows the schematic illustration of RMC samples preparation sequence. During the whole microwave synthesis preparation of MCs and RMCs, the mixers were stirred at 600 rpm. After the reactions were

complete, the products were washed, dried and annealed same as MC samples.

For the preparation of RC, the same procedure as RMC2 was applied, but MC2 was replaced by CNF as the substrate for RuO_2 deposition.

2.2. Materials characterization

The morphological and structural evaluations of the samples were performed by using the immersion mode of a focused ion beam-scanning electron microscope (FIB-SEM, FEI 600 Dual Beam) operating at 15 kV and transmission electron microscope (TEM, FEI Tecnai G2 F30) operating at 300 kV. For TEM measurements, samples were randomly dispersed in acetone and dropped on a lacy carbon coated TEM copper grid. Energy dispersive spectroscopy (EDS) was performed in SEM (FEI-Quanta 200 FEG) operating at 15 kV and the average of 6 different points measurements were used for Ru: Mn ratio calculations. The averages of diameter of more than 40 fibers from different SEM images were used for fiber diameter calculations. CHNS elemental analysis of the samples was performed by using a Thermo Flash 2000 elemental analyzer. Crystallographic identifications were performed by a Panalytical (X'pert Pro MPD) instrument and x-ray diffraction (XRD) patterns were collected over the 2θ range of $10°–80°$ using Cu-kα radiation ($\lambda = 1.54$ Å). High resolution x-ray photoelectron spectroscopy (XPS, Thermoscientific K-Alpha, Al K-Alpha radiation) was performed on MC2 and RMCs samples to determine the valence number of Mn and Raman spectra were recorded on a confocal Raman instrument (WITec alpha300).

2.3. Electrochemical measurements

All electrochemical measurements were performed with Biologic SP-150 potentiostat at room temperature. The standard three-electrode electrochemical cell was used with the glassy carbon electrode (GC, 3 mm diameter, $0.070\,68\ cm^2$ of geometric surface area), Pt spiral wire and Ag|AgCl|KCl$_{(sat.)}$ as working, counter and reference electrodes, respectively. The electrochemical characterizations were performed in 20 ml 0.1 M KOH solution where prior to each measurement the electrolyte solution was saturated with either N_2 or O_2 gas (99.999% of purity) for 30 min. More details about electrochemical measurements and electrodes preparation is available in supplementary information.

2.4. Na–O_2 cell assembly and galvanostatic measurements

Na–O_2 cells were assembled inside an Ar-filled glovebox (O_2 level < 0.5 ppm, H_2O level < 0.5 ppm) with metallic Na as anode, Celgard 2500 and GF/C as the separators and 20 wt% C65 containing CNF, MC2, RC and RMC2 cathodes. 280 μl of 0.5 M $NaCF_3SO_3$ in tetraethylene glycol dimethyl ether (H_2O amount <10 ppm according to Karl Fischer titration) was used in each cell as the electrolyte. The mass of active materials on cathodes was ~0.5 mg which were drop casted on Ni-foams (~11 mm diameter). Galvanostatic measurements of cells were performed using a battery cycler (Landt
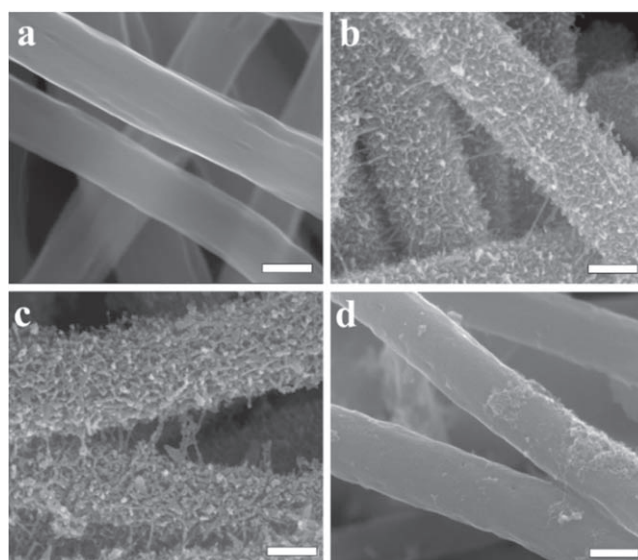

Figure 2. SEM images of (a) CNF, (b) MC2, (c) RMC2 and (d) RC (scale bars, 200 nm).

Instruments CT2001A) under 1.5 mbar of O_2 pressure (40 ml integrated O_2 tank). Discharged or charged cathodes were extracted from disassembled cells inside the glovebox and washed with 3 ml acetonitrile (H_2O amount <5 ppm) in order to remove residual electrolyte and used for postmortem characterizations.

3. Results and discussions

In order to find the optimum amount of $KMnO_4$ and $RuCl_3.xH_2O$ precursors, three different batches of MCs and RMCs are prepared and morphological and structural evaluations are performed by SEM (figures 2, S1–S3, available online at stacks.iop.org/NANO/29/475401/mmedia). The as electrospun CNF exhibits fibrous structure with smooth surface and mean diameter of 255 nm (176–382 nm) (figure 2(a)). However, drastic morphological changes were observed after Mn_2O_3 deposition on CNF (figures 2(b), S1(b) and S2). Although the CNF framework remains unchanged in MC samples, the deposition of Mn_2O_3 nano-rods turns the structure to a 3D porous platform, which become quite desirable for RuO_2 nanoparticle decoration in the next step. Also, by comparing figures 2(b) and S2, it can be figured out that Mn_2O_3 coating thickness exhibits a direct relation to $KMnO_4$ precursor amount, resulting in the fibers diameter increase from MC1 (281 nm) to MC3 (464 nm). After RuO_2 deposition, the change in Mn_2O_3 nano-rods diameter can be recognized in SEM images of RMC samples (figures 2(c) and S3) when compared to MC2. Since the least amount of $RuCl_3.xH_2O$ was used for RMC1 synthesis, its morphology is quite reminiscent of MC2 (figures S3(a) and (b)). On the other hand, some RuO_2 agglomerates existing between Mn_2O_3 nano-rods and accumulating outside of the structure are observed in RMC3 (figures S3(c) and (d)), which results in pore clogging and preventing electrolyte ion accessibility to
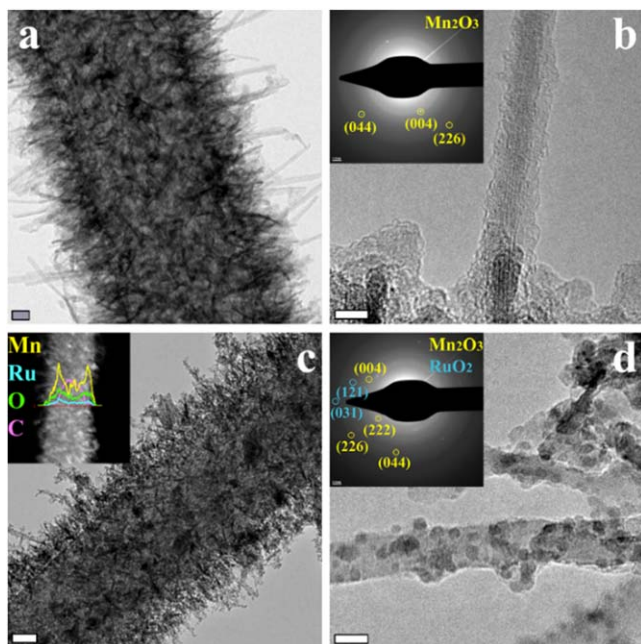
Figure 3. TEM (a), (c) and HRTEM (b), (d) images of MC2 (a), (b) and RMC2 (c), (d). Insets in (b) and (d) are the corresponding SAED pattern. Inset in (c) represents the EDS elemental line scan of RMC2 (scale bars, (a): 50 nm, (b) and (d): 5 nm, (c) and inset: 50 nm).

the inner pores. Anyhow, the surface morphology of RMC2 in figure 2(c) exhibits no agglomeration of RuO_2, showing that the RuO_2 nanoparticles were effectively deposited on Mn_2O_3 nano-rods. In order to realize the function of porous Mn_2O_3 nano-rods framework in the second hydrothermal step, as electrospun pristine CNF was used for RuO_2 deposition to make RC (figure 2(d)). It can be seen that in the absence of Mn_2O_3 nanorods, RuO_2 agglomerates are dominating in this sample. This behavior demonstrates that Mn_2O_3 nanorods act as trapping network to anchor individual RuO_2 nanoparticles which results in the uniform distribution of them in the structure.

TEM has been exploited to further investigate the nanostructure of MC2, RMC2 and RC, as shown in figures 3 and S4. The TEM and high resolution TEM (HRTEM) imaging revealed that a large number of Mn_2O_3 nano-rods are grown upright on CNF in MC2, making an open porous 3D nano-structure (figures 3(a) and (b) and S4(a)). The selected area electron diffraction (SAED) pattern of MC2 shows the characteristic diffraction rings attributed to the (004), (044) and (226) planes, indicating the crystalline nature of Mn_2O_3 nano-rods. The TEM images of RMC2 show that RuO_2 nanoparticles with the mean size of 1.57 nm are uniformly distributed on Mn_2O_3 nano-rods without any agglomeration and pore clogging, further confirming the trapping function of Mn_2O_3 nano-rods in the structure (figures 3(c), (d) and S4(b)). The formation of hierarchical RMC2 was further examined by high angle annular dark field scanning TEM images (figure S4(b)) which yielded a clear contrast between RuO_2 nanoparticles and Mn_2O_3 nano-rods. The elemental EDS line scan results (figure 3(c) inset) show the presence of O, Mn, Ru and C in the structure. The relative positions of these elements
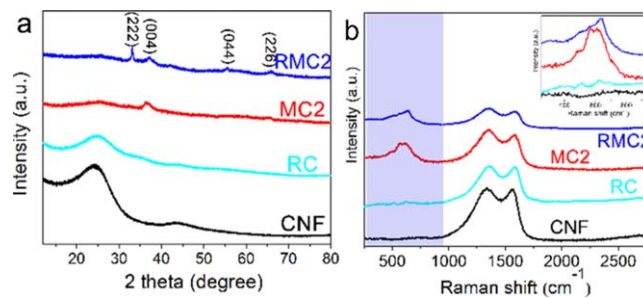

Figure 4. (a) XRD patterns and (b) Raman spectra of CNF, RC, MC2 and RMC2. Inset in (b) represents the enlarged spectra of shaded region.

indicate that O, Mn and Ru were across the whole structure, therefore, RuO_2/Mn_2O_3 has grown on the CNF core. Furthermore, SAED pattern of RMC2 (figure 3(d) inset) consists of characteristic diffraction rings of (121) and (031) planes attributed to RuO_2 and those of Mn_2O_3. The agglomerating nature of RuO_2 nanoparticles was also observed in more detail in TEM images of RC (figures S4(e) and (f)). The crystallinity of the samples was further analyzed by XRD (figures 4(a) and S5(a)). The XRD pattern of CNF shows a broad peak at $2\theta = 25°$ corresponding to the (002) plane of graphitic carbon. In the diffraction patterns of MC and RMC samples, the peaks at $2\theta = 33°$, $38.2°$, $55.4°$ and $65.8°$ are corresponding to (222), (004), (044) and (226) planes of Mn_2O_3 (ICSD 98-003-3647), respectively. It can be realized that Mn_2O_3 gets more crystalline in RMC samples compared to MC samples which can be owing to the second hydrothermal step for RuO_2 deposition. Also, no obvious peaks relating to RuO_2 were observed in the patterns of RC and RMC samples which is because of minor amount and small crystal size of RuO_2.

Figures 4(b) and S5(b) show the Raman spectra of the samples, in which there are two main peaks of CNF including D band at 1351 cm^{-1} related to the phonons with A_{1g} symmetry and G band at 1584 cm^{-1} corresponding to the E_{2g} phonon of sp^2 carbon atoms [35, 36]. The Raman spectra of MC and RMC samples exhibit three bands at 500, 560 and 620 cm^{-1} which are corresponding to the asymmetric stretching of bridging oxygen species (Mn–O–Mn) and symmetric stretch of Mn_2O_3 groups [37–39]. The Raman spectrum of RC shows two peaks at 520 and 631 cm^{-1} which are related to the first order E_g and A_{1g} phonon bands of rutile RuO_2 [40]. However, since the peaks of RuO_2 and Mn_2O_3 coincide in the same spectrum region, there is no obvious peak of RuO_2 in RMCs. The presence of RuO2 in the samples is further approved by EDS (figure S6) and XPS high resolution Ru3d spectra (figure S7) and further confirmation about Mn oxidation state of MC2 and RMCs were determined by XPS analysis (figure S5(c)). The Mn 2p spectra of all samples are mainly composed of two peaks located around ∼641.1 eV and ∼652.7 eV corresponding to Mn $2p_{3/2}$ and Mn $2p_{1/2}$ of Mn^{3+}, respectively, and two minor peaks spectra around ∼643.4 and ∼655.1 eV assigned to Mn^{4+} species [41]. The effect of mixed Mn oxidation state on the electrochemical
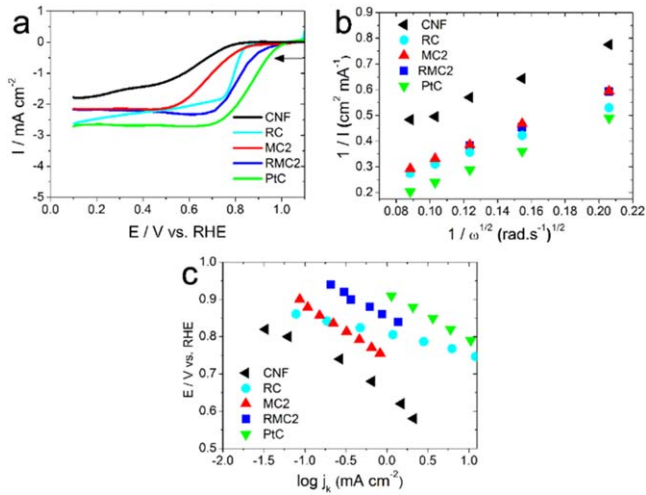
Figure 5. (a) RDE voltammograms with a sweep rate of $10\,mV\,s^{-1}$ at 400 rpm in O_2-saturated 0.1 M KOH, (b) Koutechy–Levich plots and (c) Tafel plots of CNF, RC, MC2, RMC2 and Pt/C.

behavior will be discussed in the following discussion part for the electrochemical results.

The electrocatalytic ORR activity of the prepared samples was analyzed with RDE measurements from 225 to 1225 rpm with the scan rate of $10\,mV\,s^{-1}$ in 0.1 M KOH aqueous solution (figures 5(a), S8(a) and S9). The Koutecky–Levich plots at the steady state currents were also shown in figures 5(b) and S8(b). The number of electrons involved in the ORR per oxygen molecule was determined from the slope using Koutecky–Levich equitation:

$$1/j = 1/j_k + 1/j_L = 1/j_k + 1/(B\omega^{1/2}), \tag{1}$$

where j is the measured current, j_k is the kinetic current density, j_L is the Levich current density, $B = 0.62nFCD^{2/3}v^{-1/6}$, n is the number of electrons transferred per oxygen molecule, F is the Faraday constant i.e. $96\,485\,C\,mol^{-1}$, C is the dissolved oxygen concentration in the solution ($1.26 \times 10^{-6}\,mol\,cm^{-3}$), v is the kinematic viscosity of the solution ($1.009 \times 10^{-2}\,cm^2\,s^{-1}$), D is the diffusion coefficient of oxygen ($2.1 \times 10^{-5}\,cm^2\,s^{-1}$) and ω is the rotation rate ($rad\,s^{-1}$). Assuming a four-electron reaction and the known geometric electrode surface area, the theoretical slope B is $2.5\,cm^2\,rad^{1/2}\,mA^{-1}\,s^{-1/2}$.

The kinetic current density was calculated according to the following equation:

$$j_k = (j \times j_L)/(j_L - j), \tag{2}$$

which is further used to estimate the Tafel slopes (figures 5(c) and S8(c)) to find out ORR kinetics of the catalysts. The slope and constant obtained from the straight line of $\log j_k$ versus potential were used to estimate Tafel slope and the exchange current density, respectively. Table 1 summarizes the ORR performance of the materials resulted in figures 5 and S8. The CNF synthesized from PAN in this study generates nitrogen-doped carbon fibers (table S1) which have been demonstrated as one of the suitable catalysts for ORR. It shows the number

of electrons involved in ORR as 3.4 with Tafel slope of $133\,mV\,dec^{-1}$ and onset potential of 0.87 V. However, poor stability of such carbon in energy applications needs a further coating of secondary material [42, 43].

After Mn_2O_3 coating, ca. 30 mV anodic shift in the onset potential showed further improvement in the ORR catalysis analyzed at the MC1 and MC2 catalysts. Among MC catalysts, electrocatalytic activity towards ORR clearly shows that MC2 is better in terms of most anodic onset potential with lower Tafel slope and higher $E_{1/2}$ and j_k. Although the number of electrons involved in ORR was less at MC2, better ORR and OER kinetics made it the suitable catalyst for further RuO_2 deposition. After RuO_2 deposition, RMC2 proved as the best ORR catalyst amongst all RMCs, MCs and RC samples and also comparable with Pt/C catalyst.

The Tafel slope of $121\,mV\,dec^{-1}$ at RMC2 indicates that first electron transfer is the rate-limiting step. As the RuO_2 amount increases from RMC1 to RMC2, catalysis becomes more efficient thermodynamically and kinetically, however, further increase in RuO_2 turns out to agglomeration (figures S3(c) and (d)) which again decreases the efficiency of catalysis in RMC3. The RC catalyst which showed agglomerated RuO_2 morphology in absence of Mn_2O_3 nano-rods (figures 2(d) and S4(e) and (f)) resulted in the cathodic shift of 70 mV onset potential as compared to RMC2. Thus, the ORR catalysis at RMC2 is proving the synergistic effect of Mn_2O_3 and RuO_2.

From the XPS data (figure S5(c)), it is clear that MC2 and RMC catalysts are composed of both Mn^{3+} and Mn^{4+}. Although Mn_2O_3 was predicted to be a poor catalyst for ORR [44], it has also been reported that applied potentials can change the oxidation state of manganese [45, 46]. Furthermore, some researchers showed Mn_2O_3 can also enhance ORR catalysis in the presence of another catalyst [44, 47]. Therefore, mediated electron transfer from co-catalyst may enhance the ORR catalytic activity at Mn_2O_3. Based on the earlier studies, it is proposed that ORR on MnO_2 can process through mediation involving the reduction of MnO_2 to $MnOOH$, followed by electron transfer from Mn^{3+} to oxygen [48, 49]. Takashima *et al* have reported that Mn^{3+} is stable in alkaline solution at the high potential region of OER [50]. However, in the potential window of ORR, due to applied potentials along with the presence of co-catalyst (i.e. RuO_2), the possibility of disproportionation (i.e. to form Mn^{2+} and Mn^{4+}) or reduction of the Mn^{3+} state cannot be ruled out [49–51]. Thus, following ORR mechanism can be expected on the MC and RMC catalysts directly at the MnO_2 and disproportionated or reduced Mn^{4+} surface [52]
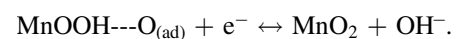
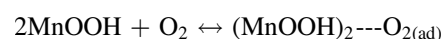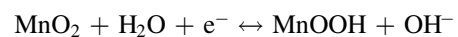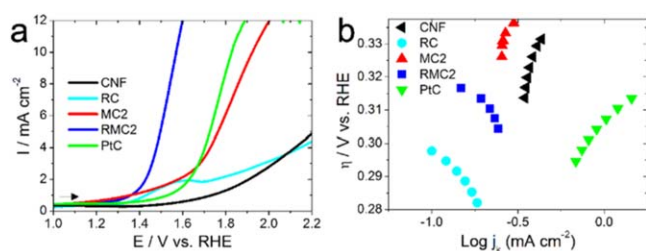$$MnO_2 + H_2O + e^- \leftrightarrow MnOOH + OH^-$$

$$2MnOOH + O_2 \leftrightarrow (MnOOH)_2\text{---}O_{2(ad)}$$

$$(MnOOH)_2\text{---}O_{2(ad)} + e^- \rightarrow MnOOH\text{---}O_{(ad)} + OH^- + MnO_2$$

$$MnOOH\text{---}O_{(ad)} + e^- \leftrightarrow MnO_2 + OH^-.$$

Sample	Onset potential V versus RHE	No. of electrons	Tafel slope mV dec^{-1}	$E_{1/2}$ at 400 rpm V versus RHE	j_k at 820 mV mA cm^{-2}	j_k at 720 mV mA cm^{-2}	i_0 mA cm^{-2}
MC1	0.90	3.81	175	0.65	0.525	1.4662	5.6885
MC2	0.90	3.34	140	0.68	0.536	1.47	5.546
MC3	0.88	3.83	177	0.62	0.295	0.979	5.163
RMC1	0.92	2.1	153	0.81	1.514	31	7.063
RMC2	0.95	3.4	121	0.825	2.168	66.94	7.178
RMC3	0.92	2.95	134	0.8	0.797	2.95	6.41
RC	0.88	3.8	49	0.8	0.555	1.22	6.41
PtC	0.98	3.9	119	0.85	5.979	70	8.222
CNF	0.87	3.4	133	0.62	0.033	0.365	4.487

Figure 6. (a) LSVs measured at a sweep rate of 10 mV s^{-1} in N$_2$-saturated 0.1 M KOH and (b) Tafel plots for CNF, RC, MC2, RMC2 and Pt/C.

Although RuO$_2$ is well known for OER, it does possess ORR catalysis through the mechanism proposed in figure S8-d [53]. The different ratios of Mn$_2$O$_3$:MnO$_2$ and change in the active state of Mn$_2$O$_3$ by applied potential are possible rationales for the difference in ORR catalytic activity along with the different amounts and morphologies of deposited Mn$_2$O$_3$ and RuO$_2$ in RMC samples.

The double-layer capacitive region is a precise indicator of an electrochemically active surface area (ECSA). The ECSA of RMCs and RC samples were estimated from the double-layer capacitance (C_{dl}) by measuring non-Faradic capacitive current from the CVs measured at different scan rates (figure S10 and figure S10 note). The ECSA was increased from RMC1 to RMC2 due to the higher loading of RuO$_2$ on RMC2 sample, but when the amount of RuO$_2$ was further increased in RMC3, ECSA and RF were decreased compared to RMC2 due to the agglomeration of RuO$_2$ nanoparticles. The effect of ECSA and roughness factor (RF) was in agreement with the electrochemical measurements of ORR and OER.

The electrocatalytic activity of the samples towards OER in 0.1 M KOH aqueous solution was measured via LSV (figures 6(a) and S11(a)) and the overpotential for OER was considered as $\eta = E$ versus RHE—1.23 V. Table 2 summarizes all parameters obtained for the samples in this part. As shown, the onset potential of OER at RMC2 ($\eta \sim 0.2$ V) is the most cathodic, indicating best OER catalytic activity among these catalysts and in good agreement with the pure RuO$_2$ and Mn-Ru oxide composite [30, 54]. As per the standard convention, 10% efficient solar water-splitting devices should operate at 10 mA cm^{-2} below $\sim$0.45 V

overpotential for combined OER and HER [55, 56]. Thus, potential required to reach this expected current density (for OER) based on geometric area was compared in table 2. The turn over frequency (TOF) value determined at an overpotential of 300 mV for RMC2 was 0.014 s^{-1}, which is consistent with the Mn-Ru-based catalysts [30] and ca. 15 fold higher than the IrO$_x$ (0.0089 s^{-1}) catalyst [57] (figure S11 note).

The kinetic parameters were measured by plotting overpotential against log (j) for all RMCs and RC samples (figures 6(b) and S11(b)), based on the fundamental equation (3):

$$\eta = a + (2.3RT/\alpha nF)\log(j), \qquad (3)$$

where j is the current density and other symbols have their usual meanings. The lower the value of the Tafel slope, better the catalytic performance with rapid kinetics. The lowest Tafel slope of 52 mV dec^{-1} was achieved for RMC2 indicating better OER kinetics compared to the other samples (table 2). According to the Zeradjanin *et al* 'cracked' RuO$_2$ films exhibited superior OER activity than the 'crack-free' structure. In other words, more exposed edges of RuO$_2$ proves better catalytic activity than the plain films [58]. Thus, it proves the importance of morphology of catalysts. Considering this phenomenon, deposition of nanoparticles of RuO$_2$ is preferred in this work so that, the nanoparticle surface acts like the cracked surface of RuO$_2$ film to increase efficient catalytically active sites towards OER. Our results further confirm this hypothesis where RMC2 was superior over RMC3 and RC which have agglomerated RuO$_2$ nanoparticles, thus, reducing the edges or catalytically active sites. In addition, better OER catalysis of RMC2 over RMC1 is expected due to the high amount of RuO$_2$ in RMC2. The overall reaction at the RuO$_2$ is elaborated in figure S11(c) as proposed earlier for the bimetallic composites [55]. Another possibility of the cathodic shift in the onset potential of OER might be due to the contribution from Mn^{3+} which is stable in an alkaline medium which proved to be effective OER catalyst. The SEM and TEM images of RMC samples clearly shows that RuO$_2$ forms nanoparticles with partially covering the surface of Mn$_2$O$_3$, in other words, uncovered surface of Mn$_2$O$_3$ can act as the sites for OER catalytic reactions. Takashima *et al* have reported that in the alkaline solution

Table 2. Electrochemical parameters of catalysts towards OER in 0.1 M KOH.

| Sample	ESCA/cm^2	RF	Onset η/V	η to 10 mA cm^{-2}/V	Tafel slope/mV dec^{-1}	TOF/s^{-1}	j_g at 0.34 V mA^{-1} cm^{-2}	j_s/mA cm^{-2}	Mass activity/mA g^{-1}
MC1	—	—	0.5	1.13	124	—	—	—	—
MC2	—	—	0.45	0.69	113	0.003 58	1.95	—	8758.417
MC4	—	—	0.45	0.919	166	—	—	—	—
RMC21	67.2	950.76	0.25	0.47	63	0.005 77	5.57	0.0056	14 258.55
RMC22	67.7	957.83	0.2	0.34	52	0.014 17	10.05	0.0105	36 255.14
RMC23	54.5	771.08	0.27	0.36	55	0.008 48	8.87	0.0115	22 406.08
RC	56.8	803.62	0.2	—	58	0.007 75	1.87	0.002 32	22 496.1
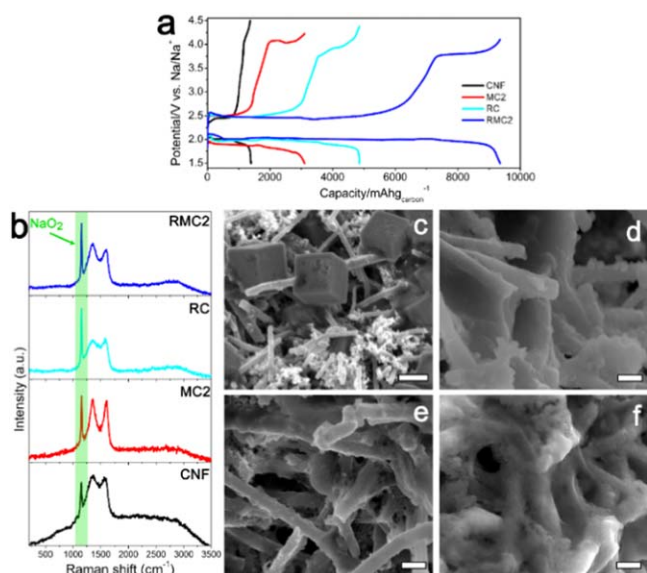
Figure 7. (a) Galvanostatic discharge/charge plots of CNF, MC2, RC and RMC2 at a current density of 0.05 mA cm^{-2}, (b) corresponding Raman spectra of the samples at the end of discharge. The dominance of the strong peaks in the Raman spectra at 1156 cm^{-1} (highlighted spectrum) indicates deposition of NaO$_2$ as the main discharge product at the end of discharge. SEM images of (c) CNF, (d) MC2, (e) RC and (f) RMC2 discharged cathodes. Scale bars represent: (c) 1.5 μm and (d)–(f) 500 nm. Conformal distribution of NaO$_2$ on MC2, RC and RMC2 indicates the catalytic reaction throughout the whole structures.

(typically more than pH 9) Mn^{3+} ions are free from the disproportionation reaction and stabilized by a symproportionation reaction at high pH using *in situ* spectroscopic determination [50]. Furthermore, Browne *et al* also speculated it might be one of the reasons for OER catalytic enhancement at the Mn/Ru complex [30]. Thus, Mn^{3+} can catalyze OER through the stable symproportionation reaction. Although Mn^{3+} is also acting as OER catalyst, in comparison with MC samples, RMCs show the cathodic shift in the onset potential which clearly shows that contribution of RuO$_2$ nanoparticle edges is higher than the Mn^{3+} catalyst.

Till the date, IrO$_x$ and RuO$_2$ are considered as the most favorable state-of-the-art catalysts for the OER. Note that the overpotential required to achieve 10 mA cm^{-2} of RMC2 (340 mV) is 20 mV anodic to the IrO$_x$ (320 mV) and better than RuO$_2$ (390 mV) [56, 59]. Therefore, overall enhancement in the catalytic activity of RMC samples was expected as the synergistic effect of Mn$_2$O$_3$ and RuO$_2$ towards the ORR and OER.

In the light of practical applications in non-aqueous media and in order to further confirm excellent synergistic effect in RMC sample, the prepared materials were utilized in Na–O$_2$ cells as the cathode electrodes. Galvanostatic discharge/charge tests at 0.05 mA cm^{-2} (figure 7(a)) indicate the higher specific capacity For RMC2 (9352 mAh g_{carbon}^{-1}) compared with CNF (1395 mAh g_{carbon}^{-1}), MC2 (3108 mAh g_{carbon}^{-1}) and RC (4859 mAh g_{carbon}^{-1}) at the end of discharge with the cutoff potential of 1.5 V. The following charging profiles consist of two main plateaus at lower ($\sim$2.4 V) and higher

($\sim$4 V) potentials which are assigned to the decomposition of NaO$_2$ and the side products (mainly Na$_2$CO$_3$), respectively [60]. According to the overall discharge/charge measurements, RMC2 not only exhibits higher specific capacity by promoting the formation and decomposition of NaO$_2$, it also facilitates side products decomposition during charge at lower potential (3.838 V) compared to CNF (4.226 V), MC2 (4.077 V) and RC (3.963 V). In order to have a better understanding of the nature of discharge product, Raman spectroscopy of the samples at the end of discharge was investigated (figure 7(b)). The dominance of the Raman band at 1156 cm^{-1} confirms the deposition of NaO$_2$ as the main discharge product during ORR [4, 61]. However, drastic morphological differences of deposited NaO$_2$ were observed between discharged CNF and the other discharged cathodes (figures 7(c)–(f) and S12). Figures 7(c) and S12 and (e) show that micron-sized cubic NaO$_2$ particles are deposited at CNF cathode after discharge, compatible with the report of Hartmann *et al* [61, 62]. By incorporating Mn$_2$O$_3$ and/or RuO$_2$ on CNF, no further cubic particle was observed on the discharged cathodes (figures 7(d)–(f) and S12), instead, the samples were buried under a conformal coating of NaO$_2$. This behavior is well understood in Li–O$_2$ batteries in which the morphology of Li$_2$O$_2$ discharge product is transformed from conventional toroidal particles to film coating by introducing catalyst on the surface of carbonaceous backbones [63, 64]. In fact, this change is ascribed to the favored adsorption energy of peroxide and superoxide species on the surface of catalyst as the discharge product nucleation spots and the following growth [65, 66]. Therefore, the catalytic reaction can be performed throughout the entire 3D RMC structure rather than only in some local regions as observed in CNF. There is no precipitate observed in the SEM images of the cathodes after charging, indicating that the cathodes have reversibly recovered their structures at the end of complete discharge/charge cycle (figure S13). All of the above mentioned results confirm that RMC is an efficient catalyst for both aqueous and non-aqueous media.

4. Conclusions

In this study, a highly effective 3D RuO$_2$/Mn$_2$O$_3$/CNF ternary composite has been prepared and used as the bifunctional electrocatalyst for ORR/OER. Three sets of Mn$_2$O$_3$/CNF composites with different Mn$_2$O$_3$ amounts are prepared by a microwave synthesis method and according to the electrochemical results towards ORR/OER, the composite with medium amount of Mn$_2$O$_3$ is selected for RuO$_2$ deposition in the second microwave synthesis step. The RuO$_2$/Mn$_2$O$_3$/CNF composite demonstrated superior ORR/OER activity compared to the other samples prepared in this work and state of the art RuO$_2$ and IrO$_x$ type materials. In order to validate the applicability of the catalyst in non-aqueous media, the catalysts were used as cathode materials in Na–O$_2$ cells and RuO$_2$/Mn$_2$O$_3$/CNF showed 6.7 fold specific capacity as CNF. This enhancement is attributed to the synergistic effect of highly electronically conductive CNF

core and RuO_2–Mn_2O_3 shell, as well as the novel 3D morphology of the composite. The more exposed edges and uniform distribution of RuO_2 nano-particles in RuO_2/Mn_2O_3/CNF is due to the trapping effect of Mn_2O_3 nano-rods, which is confirmed by TEM and SEM results. The 3D design of Mn_2O_3–RuO_2 which are of mostly known catalysts for ORR and OER, respectively, is introduced for the first time in this work, to achieve highly active bi-functional catalyst for ORR and OER.

ORCID iDs

Mohammad Fathi Tovini ⬤ https://orcid.org/0000-0003-4334-4471
Bhushan Patil ⬤ https://orcid.org/0000-0003-1659-4715
Tamer Uyar ⬤ https://orcid.org/0000-0002-3989-4481

References

[1] Knudsen K B, Nichols J E, Vegge T, Luntz A C, McCloskey B D and Hjelm J 2016 *J. Phys. Chem.* C **120** 10799
[2] Jiang H R, Wu M C, Zhou X L, Yan X H and Zhao T S 2016 *J. Power Sources* **325** 91
[3] Zhao N and Guo X 2015 *J. Phys. Chem.* C **119** 25319
[4] Kim J, Park H, Lee B, Seong W M, Lim H-D, Bae Y, Kim H, Kim W K, Ryu K H and Kang K 2016 *Nat. Commun.* **7** 10670
[5] Reeve Z E M, Franko C J, Harris K J, Yadegari H, Sun X and Goward G R 2017 *J. Am. Chem. Soc.* **139** 595
[6] Landa-Medrano I, Pinedo R, Bi X, Ruiz de Larramendi I, Lezama L, Janek J, Amine K, Lu J and Rojo T 2016 *ACS Appl. Mater. Interfaces* **8** 20120
[7] Sayed S Y, Yao K P C, Kwabi D G, Batcho T P, Amanchukwu C V, Feng S, Thompson C V and Shao-Horn Y 2016 *Chem. Commun.* **52** 9691
[8] Zhang J, Guo C, Zhang L and Li C M 2013 *Chem. Commun.* **49** 6334
[9] McCloskey B D, Garcia J M and Luntz A C 2014 *J. Phys. Chem. Lett.* **5** 1230
[10] Toh R J, Sofer Z and Pumera M 2015 *ChemPhysChem* **16** 3527
[11] Su H-Y, Gorlin Y, Man I C, Calle-Vallejo F, Norskov J K, Jaramillo T F and Rossmeisl J 2012 *Phys. Chem. Chem. Phys.* **14** 14010
[12] Ye D, Wu T, Cao H, Wang Y, Liu B, Zhang S and Kong J 2015 *RSC Adv.* **5** 26710
[13] Cao Y L, Yang H X, Ai X P and Xiao L F 2003 *J. Electroanal. Chem.* **557** 127
[14] Gyenge E L and Drillet J-F 2011 *J. Electrochem. Soc.* **159** F23
[15] Lv X, Lv W, Wei W, Zheng X, Zhang C, Zhi L and Yang Q-H 2015 *Chem. Commun.* **51** 3911
[16] Li L, Hu Z A, An N, Yang Y Y, Li Z M and Wu H Y 2014 *J. Phys. Chem.* C **118** 22865
[17] Liu M, Gan L, Xiong W, Xu Z, Zhu D and Chen L 2014 *J. Mater. Chem.* A **2** 2555
[18] Zhao C-F, Lu K and Ma H 2016 *RSC Adv.* **6** 107638
[19] Kuo C-H, Li W, Pahalagedara L, El-Sawy A M, Kriz D, Genz N, Guild C, Ressler T, Suib S L and He J 2015 *Angew. Chem.* **127** 2375
[20] Frydendal R, Paoli E A, Chorkendorff I, Rossmeisl J and Stephens I E L 2015 *Adv. Energy Mater.* **5** 1500991
[21] Li N, Xia W-Y, Wang J, Liu Z-L, Li Q-Y, Chen S-Z, Xu C-W and Lu X-H 2015 *J. Mater. Chem.* A **3** 21308
[22] Xie K, Masa J, Madej E, Yang F, Weide P, Dong W, Muhler M, Schuhmann W and Xia W 2015 *ChemCatChem* **7** 3027
[23] Gorlin Y and Jaramillo T F 2010 *J. Am. Chem. Soc.* **132** 13612
[24] Hu X, Cheng F, Zhang N, Han X and Chen J 2015 *Small* **11** 5545
[25] Jung H-G, Jeong Y S, Park J-B, Sun Y-K, Scrosati B and Lee Y J 2013 *ACS Nano* **7** 3532
[26] Jian Z, Liu P, Li F, He P, Guo X, Chen M and Zhou H 2014 *Angew. Chem., Int. Ed. Engl.* **53** 442
[27] Lee Y, Suntivich J, May K J, Perry E E and Shao-Horn Y 2012 *J. Phys. Chem. Lett.* **3** 399
[28] Bhowmik T, Kundu M K and Barman S 2016 *ACS Appl. Mater. Interfaces* **8** 28678
[29] Yoon K R, Lee G Y, Jung J-W, Kim N-H, Kim S O and Kim I-D 2016 *Nano Lett.* **16** 2076
[30] Xu Y-F, Chen Y, Xu G-L, Zhang X-R, Chen Z, Li J-T, Huang L, Amine K and Sun S-G 2016 *Nano Energy* **28** 63
[31] Browne M P, Nolan H, Duesberg G S, Colavita P E and Lyons M E G 2016 *ACS Catal.* **6** 2408
[32] Zhu J *et al* 2016 *Nat. Commun.* **7** 13432
[33] Mazloumi M, Shadmehr S, Rangom Y, Nazar L F and Tang X 2013 *ACS Nano* **7** 4281
[34] Wan Y, Yang Z, Xiong G, Guo R, Liu Z and Luo H 2015 *J. Power Sources* **294** 414
[35] Lee J S, Lee C, Jun J, Shin D H and Jang J 2014 *J. Mater. Chem.* A **2** 11922
[36] Li W, Zhang L-S, Wang Q, Yu Y, Chen Z, Cao C-Y and Song W-G 2012 *J. Mater. Chem.* **22** 15342
[37] Xu J, Gao Q, Zhang Y, Tan Y, Tian W, Zhu L and Jiang L 2014 *Sci. Rep.* **4** 5545
[38] Luo Y, Deng Y-Q, Mao W, Yang X-J, Zhu K, Xu J and Han Y-F 2012 *J. Phys. Chem.* C **116** 20975
[39] Han Y-F, Chen F, Zhong Z, Ramesh K, Chen L and Widjaja E 2006 *J. Phys. Chem.* B **110** 24450
[40] Ren Q, Wang R, Wang H, Key J, Brett D J L, Ji S, Yin S and Shen P K 2016 *J. Mater. Chem.* A **4** 7591
[41] Kim Y L, Choi H-A, Lee N-S, Son B, Kim H J, Baik J M, Lee Y, Lee C and Kim M H 2015 *Phys. Chem. Chem. Phys.* **17** 7435
[42] Hou J, Li Y, Mao M, Ren L and Zhao X 2014 *ACS Appl. Mater. Interfaces* **6** 14981
[43] Lu J *et al* 2013 *Nat. Commun.* **4** 2383
[44] Ottakam Thotiyl M M, Freunberger S A, Peng Z, Chen Y, Liu Z and Bruce P G 2013 *Nat. Mater.* **12** 1050
[45] Mao L, Zhang D, Sotomura T, Nakatsu K, Koshiba N and Ohsaka T 2003 *Electrochim. Acta* **48** 1015
[46] Jahan M, Tominaka S and Henzie J 2016 *Dalton Trans.* **45** 18494
[47] Kozawa A and Powers R A 1966 *J. Electrochem. Soc.* **113** 870
[48] Gorlin Y, Chung C-J, Nordlund D, Clemens B M and Jaramillo T F 2012 *ACS Catal.* **2** 2687
[49] Lima F H B, Calegaro M L and Ticianelli E A 2007 *Electrochim. Acta* **52** 3732
[50] Tang Q, Jiang L, Liu J, Wang S and Sun G 2014 *ACS Catal.* **4** 457

[51] Takashima T, Hashimoto K and Nakamura R 2012 *J. Am. Chem. Soc.* **134** 1519

[52] Cheng F, Zhang T, Zhang Y, Du J, Han X and Chen J 2013 *Angew. Chem., Int. Ed. Engl.* **52** 2474

[53] Valim R B, Santos M C, Lanza M R V, Machado S A S, Lima F H B and Calegaro M L 2012 *Electrochim. Acta* **85** 423

[54] Prakash J and Joachin H 2000 *Electrochim. Acta* **45** 2289

[55] Godwin I J, Doyle R L and Lyons M E G 2014 *J. Electrochem. Soc.* **161** F906

[56] Walter M G, Warren E L, McKone J R, Boettcher S W, Mi Q, Santori E A and Lewis N S 2010 *Chem. Rev.* **110** 6446

[57] McCrory C C L, Jung S, Peters J C and Jaramillo T F 2013 *J. Am. Chem. Soc.* **135** 16977

[58] Trotochaud L, Ranney J K, Williams K N and Boettcher S W 2012 *J. Am. Chem. Soc.* **134** 17253

[59] Zeradjanin A R, Topalov A A, Van Overmeere Q, Cherevko S, Chen X, Ventosa E, Schuhmann W and Mayrhofer K J J 2014 *RSC Adv.* **4** 9579

[60] Sun Q *et al* 2017 *Adv. Funct. Mater.* **27** 1606662

[61] Hartmann P, Bender C L, Vračar M, Dürr A K, Garsuch A, Janek J and Adelhelm P 2013 *Nat. Mater.* **12** 228

[62] Hartmann P, Bender C L, Sann J, Durr A K, Jansen M, Janek J and Adelhelm P 2013 *Phys. Chem. Chem. Phys.* **15** 11661

[63] Yilmaz E, Yogi C, Yamanaka K, Ohta T and Byon H R 2013 *Nano Lett.* **13** 4679

[64] Yang Y, Zhang T, Wang X, Chen L, Wu N, Liu W, Lu H, Xiao L, Fu L and Zhuang L 2016 *ACS Appl. Mater. Interfaces* **8** 21350

[65] Yang Y *et al* 2017 *ACS Appl. Mater. Interfaces* **9** 19800

[66] Krishnamurthy D, Hansen H A and Viswanathan V 2016 *ACS Energy Lett.* **1** 162